System Parameter Design of Multimodal Small Satellite SARs Operating in Scan Mode and Transmit Power Optimization for Marine Scenes

PENG ZHOU[1], (Member, IEEE), **WEIQIANG LV**[1], **ZHENHUA ZHANG**[2], **YING WANG**[2], **XI ZHANG**[3], AND **YONGSHOU DAI**[1]
[1]College of Oceanography and Space Informatics, China University of Petroleum, Qingdao 266580, China
[2]Beijing Research Institute of Telemetry, Beijing 100076, China
[3]First Institute of Oceanography, Ministry of Natural Resources of the People's Republic of China, Qingdao 266061, China

Corresponding author: Peng Zhou (zhoupeng@upc.edu.cn)

ABSTRACT Multimodal small satellite synthetic aperture radar (SAR) is a new radar system under development that integrates an SAR, altimeter, scatterometer, and spectrometer. When applied to marine scenes, this system can be used to measure both marine targets and marine dynamic environments with high precision. This study addresses system parameter design for multimodal small satellite SAR operating in scan mode, and this design provides system parameters such as antenna size, signal bandwidth, pulse repetition frequency, scanning wavenumber and wave position for system simulation in scan mode. A method for optimizing the transmit power when illuminating a marine scene based on the wind speed and wind direction above the sea surface is studied. The goal is to fully use the characteristics of strong sea surface microwave scattering under a suitable wind speed and wind direction to reduce the required transmit power, thus improving the available data sampling time per orbit of a multimodal radar when working in SAR mode. Various simulation experiments were conducted, and the system parameter design results are given under scan mode. Furthermore, imaging simulation results of ocean scenes are also given under conventional and decreased power after optimization. The results show that good ocean scene imaging results are obtained when the designed system parameters are used for system simulation. In addition, the simulation results also verify that when the sea surface wind speed is relatively high and the wind direction is suitable, an acceptable ocean scene imaging result can still be obtained by using reduced transmit power.

INDEX TERMS Multimodal small satellite SAR, scan mode, system parameter design, ocean scene imaging simulation, transmission power optimization.

I. INTRODUCTION

Multimodal small satellite synthetic aperture radar (SAR) is a new radar system under development [1] that simultaneously takes full advantage of the characteristics of two-dimensional phased array antennas such as flexible beam scanning and multiple beam generation [2] and the flexibility of recon-

The associate editor coordinating the review of this manuscript and approving it for publication was Gerardo Di Martino.

figurable electronic devices introduced by software reconfigurable technology [3]–[5]. This system integrates remote sensor functions including an SAR, altimeter, scatterometer and spectrometer by a software-reconfigurable radar receiver and by steering the antenna side looking with a medium incidence angle, nadir looking, rotating 360 degrees horizontally with a medium incidence angle and switching between two different incidence angles, and rotating 360 degrees horizontally with a small incidence angle, respectively.

More specifically, the system can work in different modes including the SAR, altimeter, scatterometer, and spectrometer under a time-sharing mechanism by receiving remote control instructions from ground stations. When applied to marine scenes, SAR mode has obvious advantages in detecting marine targets [6]; altimeter mode measures sea surface height with high precision; scatterometer mode is good at retrieving sea surface wind field information with high precision [7], [8]; and spectrometer mode has unique advantages for retrieving wave spectrum information and extracting wave parameters [9]. Because each operating mode has its own advantages, this new radar system can both detect marine targets and measure marine dynamic environments with high precision; thus, it has good development prospects. In addition, a laser communication terminal can be installed on the multimodal small satellite SAR to enable multiple satellites to communicate, thus achieving synchronous multistatic observations to improve the remote sensing performance such as achieving high-resolution wide-swath microwave images and obtaining high-precision information of marine targets and marine dynamic environments simultaneously, or achieving network observations through satellite constellations to improve the temporal resolution. Furthermore, to deal with the limited processing resources of a small satellite, the real-time processing capability of a small satellite can be effectively improved through inter-satellite parallel computing with the support of high-speed inter-satellite communication. Due to the rapid development of electronic equipment technology, the size and cost of phased array antennas and laser communication devices are continuously decreasing [10], [11], making it possible to manufacture the multimodal small satellite SARs described in this paper.

As a new radar system under development, multimodal small satellite SAR needs to be simulated by computers, which is an important means for carrying out early research. This paper focuses primarily on imaging simulations and transmission power optimization of ocean scenes when multimodal small satellite SAR is working in scan mode. In SAR system simulations, operating parameters such as antenna size, signal bandwidth, pulse repetition frequency (PRF), scanning wavenumber and wave position should be determined first [12]. Due to the size and load limitations of small satellites, the parameters of traditional spaceborne SAR cannot be directly used in determining the operating parameters of multimodal small satellite SAR; therefore, specific designs are required. After the design results for the operating parameters of the multimodal small satellite SAR system are obtained, ocean scene imaging simulations can be further carried out. Due to transmit power limitations and power consumption, the available data sampling time of spaceborne SAR is usually only a few minutes per orbit [13], and the available data sampling time of multimodal small satellite SAR is even shorter when working in SAR mode. A multimodal small satellite SAR working in scatterometer mode can obtain the wind direction and wind speed of the irradiated sea area with high precision, and can transmit that information to other small satellites that are synchronously observing the scene. When the acquired wind speed is high and the wind direction is suitable, the microwave scattering intensity of the irradiated sea area will be strong. Here, a suitable wind direction means directions apart from those that deviate from the radar line of sight by approximately ± 90 degrees since the microwave scattering is relatively weak when the wind direction is perpendicular to the radar line of sight [14]. In this case, the emission power of the small satellite SAR can be decreased, thus increasing the available data-sampling time per orbit of SAR mode.

There are numerous studies on the design of system parameters for SAR working in strip and spotlight modes. In [15] the design process of system parameters in strip mode was introduced, and [16] discusses the design of key system parameters for a high-resolution wide geosynchronous orbit (GEO)/low earth orbit (LEO) bistatic SAR system. The authors of [17] introduced software for parameter design and simulation of a spaceborne strip SAR system. The software can complete the parameter design and perform echo and imaging simulations for the strip SAR system. In [18], a design method for system parameters in spotlight mode was introduced that analyzes the factors influencing system design from several aspects, such as large distance migration, PRF selection, and antenna pattern design. However, there are relatively few studies on system parameter design for SAR working in scan mode. The details and a comprehensive discussion on the performance parameters and design constraints of scan SAR were provided in [19], including the scanning period, resolution, number of wave positions, antenna area, swath width, average transmit power and echo data rate, but that study did not reveal how to determine the position and time parameters of different subswaths, nor did it consider transmit power optimization.

In this paper, a method for designing system parameters, imaging simulations of ocean scenes and a method for optimizing the transmit power based on sea surface wind speed and direction are studied for multimodal small satellite SAR working in scan mode. Part II introduces the details for small satellite SAR system design in scan mode. Part III introduces the method for optimizing the transmit power based on the wind speed and direction above the sea surface when the multimodal small satellite SAR illuminates marine scenes. Part IV introduces the simulation process and the imaging results for small satellite SAR over ocean scenes operating in scan mode, including the adopted sea surface simulation method, echo simulation and imaging processing method, system parameter design results using the proposed method, and ocean scene simulation results under both conventional power and decreased power after using the proposed method for transmit power optimization. Part V concludes this paper.

II. PARAMETER DESIGN METHOD FOR SMALL SATELLITE SAR SYSTEMS OPERATING IN SCAN MODE

When designing the system parameters for small satellite SAR in scan mode, system operating parameters such as antenna size, signal bandwidth, PRF, scanning wavenumber, positions and the time relation of each subswath need to be determined [20], [21]. To determine the above operating parameters, other parameters such as the range resolution, azimuth resolution, swath width, satellite orbit height, satellite speed, carrier frequency, view angle range, noise figure of the receiver, and pulse width are usually known or given according to the user requirements.

First, the number of scanning wave positions is determined. The number of scanning wave positions is related to the scanning time of each subswath (i.e., the full aperture imaging accumulation time corresponding to the beam width) and the beam dwell time (i.e., the continuous imaging time of a burst within a certain subswath).

Let k represent the index of a given subswath; then, the scanning time and beam dwell time corresponding to the k-th subswath are

$$T_{Fk} = \frac{\lambda R_k}{v_g l_a} \tag{1}$$

$$T_{Dk} = \frac{\lambda R_k N_L}{2 v_s \rho_a} \tag{2}$$

respectively, where λ is the wavelength, R_k is the distance from the antenna to the center of the given subswath, v_g is the satellite's velocity relative to the ground, l_a is the azimuth antenna length, v_s is the orbit speed of the SAR, ρ_a is the azimuth resolution, and N_L is the effective multiple view number.

Dividing the scanning time corresponding to the nearest subswath by the beam dwell time corresponding to the farthest subswath is used to calculate the number of wave positions, N_B:

$$N_B = \frac{v_s}{v_g} \frac{R_N}{R_F} \frac{\rho_a/N_L}{D_a/2} \approx \frac{\rho_a/N_L}{D_a/2}$$

$$N_B = \frac{v_s}{v_g} \frac{R_N}{R_F} \frac{\rho_a/N_L}{l_a/2} \approx \frac{\rho_a/N_L}{l_a/2}, \tag{3}$$

where R_N and R_F represent the nearest and farthest slant ranges, respectively.

In equation (3), for a given ρ_a and a given N_L, the product $N_B l_a$ will be a constant, and a compromise should be made between l_a and N_B during the design process.

The second step is to determine the position of each subswath. The relation between the view angle, the incidence angle and the geocentric angle of a given subswath center is

$$\frac{\sin \gamma}{R_e} = \frac{\sin(\pi - \alpha)}{R_e + H}, \tag{4}$$

$$\varphi = \alpha - \gamma \tag{5}$$

where R_e is the radius of the earth, H is the height of the satellite, γ is the view angle, α is the incidence angle, and φ

is the geocentric angle. From equations (4) and (5), we can see that we need to know only one of the angles to calculate the other two.

For the first subswath, the view angle γ_1 is known, and the geocentric angle φ_1 can be calculated. Let φ_{a1} and φ_{b1} denote the geocentric angles corresponding to the nearest distance R_{n1} and the farthest distance R_{f1} of the first subswath, respectively. These values can be calculated as follows:

$$\varphi_{a1} = \frac{\varphi_1 R_e - 0.5 A_1 B_1}{R_e} \tag{6}$$

$$\varphi_{b1} = 2\varphi_1 - \varphi_{a1}, \tag{7}$$

where $A_1 B_1$ is the width of the first subswath, whose value can be estimated by the user requirements of the imaging swath and N_B.

After obtaining φ_{a1} and φ_{b1}, the nearest distance R_{n1} and the farthest distance R_{f1} corresponding to the first subswath can be calculated as follows:

$$R_{n1} = \sqrt{R_e^2 + (R_e + H)^2 - 2R_e(R_e + H)\cos\varphi_{a1}} \tag{8}$$

$$R_{f1} = \sqrt{R_e^2 + (R_e + H)^2 - 2R_e(R_e + H)\cos\varphi_{b1}}. \tag{9}$$

The beam width θ_1 of the first subswath is calculated by

$$\frac{\sin(\gamma_1 - 0.5 \cdot \theta_1)}{R_e} = \frac{\sin\varphi_{a1}}{R_{n1}}. \tag{10}$$

The widths of the first and second subswaths should generally overlap by one tenth. Thus,

$$A_2 B_1 = 10\% * A_1 B_1, \tag{11}$$

where $A_2 B_1$ is the intersection width between the first and second subswaths.

Assuming that the initial value of the view angle of the second subswath is $\hat{\gamma}_2$, the width of the overlap region $\widehat{A_2 B_1}$ can be calculated by

$$\widehat{A_2 B_1} = \left[\varphi_{b1} - (\hat{\alpha}_2 - \hat{\gamma}_2)\right] R_e + \frac{R_x R_e}{2(R_e + H)\sin\hat{\gamma}_2}, \tag{12}$$

where R_x is the width in the slant range direction, and its relationship with $A_2 B_1$ is

$$R_x = A_2 B_1 \cdot \sin\hat{\alpha}_2, \tag{13}$$

where $\hat{\alpha}_2$ is the incident angle corresponding to $\hat{\gamma}_2$. Obviously, the estimated view angle of the second subswath to meet the accuracy requirement can be obtained by using the iterative method. Thus, the position of the second subswath can be further determined. The positions of the other subswaths can be calculated similarly.

In step 3, the signal bandwidth B_r can be determined according to the user requirement of the range resolution ρ_{gr} by

$$B_r = \frac{C}{2\rho_{gr}\sin\alpha_{a1}}, \tag{14}$$

where C is the speed of light, and α_{a1} is the incident angle corresponding to φ_{a1} (i.e., the incident angle at the nearest end).

The 4th step involves calculating the minimum antenna area:

$$A_{min} = \frac{8 v_s \lambda R_{f,max}}{C} tan\theta_{f,max}, \quad (15)$$

where $R_{f,max}$ is the farthest distance and $\theta_{f,max}$ is the farthest incident angle.

Step 5 determines the scanning time T_{FK}, the dwell time T_{DK} and the regression time T_{RK} of each subswath. Here, the regression time T_{RK} refers to the time interval between two bursts of a certain subswath, and T_{FK} and T_{DK} are calculated by (1) and (2), respectively, while T_{RK} is calculated by

$$T_{Rk} = \frac{T_{Fk} - T_{Dk}}{N_L}. \quad (16)$$

In the 6-th step, the PRF value and the number of PRF samples in each subswath are determined. To reduce azimuth ambiguity, the *PRF* of the *k*-th subswath should satisfy

$$PRF_k \geq B_p, \quad (17)$$

where PRF_k represents the PRF value of the *k*-th subswath, B_p is the Doppler bandwidth and $B_p = v_s/\rho_a$. To reduce range ambiguity, the *PRF* of the *k*-th subswath should meet the following requirements:

$$\frac{m \cdot C}{2 R_{nk}} \leq PRF_k \leq \frac{(m+1)C}{2 R_{fk}}, \quad (18)$$

where *m* represents the number of pulses between the scene echo and the transmitted pulse and R_{nk} and R_{fk} represent the nearest and farthest distances corresponding to the *k*-th subswath, respectively.

After obtaining the *PRF* range, the timing diagram can be drawn. The X axis of the timing diagram is the *PRF* range and the Y axis is the range of the incident angles. Among these, to avoid interference from the emission pulse, the following requirements must be met:

$$\begin{cases} \dfrac{Frac(2 R_{nk} PRF_k/C)}{PRF_k} > T_r + \tau_g \\ \dfrac{Frac(2 R_{fk} PRF_k/C + T_r)}{PRF_k} < PRI_k - \tau_g \\ Int(2 R_{fk} PRF_k/C + T_r) = Int(2 R_{nk} PRF_k/C), \end{cases} \quad (19)$$

where the function Frac() represents obtaining the fractional part of the variable, the function Int() represents obtaining the integer part of the variable, T_r is the pulse width, PRI_k is the pulse repetition interval corresponding to the *k*-th subswath, and τ_g is the receiver protection time. To avoid interference from the nadir echo, it is necessary to satisfy:

$$\begin{cases} 2\dfrac{H}{C} - \dfrac{l}{PRF_k} + 2 T_r < 2\dfrac{R_{nk}}{C} - \dfrac{m}{PRF_k} \\ or \\ 2\dfrac{H}{C} - \dfrac{l}{PRF_k} > 2\dfrac{R_{fk}}{C} + T_r - \dfrac{m}{PRF_k}, \end{cases} \quad (20)$$

where *l* represents the number of pulses between the nadir echo and the transmitted pulse. After drawing the timing diagram, the *PRF* value suitable for each subswath can be

selected. The number of azimuth samples in each burst of each subswath can be obtained by dividing the beam dwell time by the value of PRI.

Step 7 verifies the range ambiguity to signal ratio $RASR_k$ and the azimuth ambiguity to signal ratio $AASR_k$ of each subswath. The formula for $RASR_k$ is

$$R_{kij} = R_{ki} + \frac{j}{2 \cdot PRF_k} \cdot C$$

$$S_{ki} = \frac{G_{kij}^2}{R_{kij}^3 \sin(\theta_{kij})}, j = 0$$

$$S_{kai} = \sum_{j=-n_1}^{n_2} \frac{G_{kij}^2}{R_{kij}^3 \sin(\theta_{kij})}, j \neq 0$$

$$G_{kij} = \left[\frac{\sin\left[\pi \cdot l_r \sin(\phi_{kij})/\lambda\right]}{\pi \cdot l_r \sin(\phi_{kij})/\lambda} \right]^2$$

$$RASA_k = \sum_{i=1}^{N_k} S_{kai} / \sum_{i=1}^{N_k} S_{ki}, \quad (21)$$

where *i* is the serial number of the range cell in the main beam, *j* is the serial number of the ambiguity region, R_{ki} is the slant range corresponding to the *i*-th range cell in the main beam, and R_{kij} is the slant range corresponding to the *j*-th ambiguity region of the *i*-th range cell in the main beam, and S_{ki} and S_{kai} are the signal power and the ambiguity power of the *i*-th range cell of the *k*-th subswath, respectively. G_{kij} and θ_{kij} are the antenna gain and the incident angle corresponding to the *j*-th ambiguity region of the *i*-th range cell of the *k*-th subswath, respectively, n_1 and n_2 are the lower limit serial number of the near-end ambiguity region and the upper limit serial number of the far-end ambiguity region respectively, and ϕ_{kij} is the angle between the beam center direction and the *j*-th ambiguity region of the *i*-th range cell of the *k*-th subswath. Here, l_r is the antenna size in the range direction, and N_k is the number of range cells in the *k*-th subswath. The formula for $AASR_k$ is

$$G(f) = \left[\frac{\sin\left(\pi l_a \frac{f}{v_s}\right)}{\pi l_a \frac{f}{v_s}} \right]^2 \quad (22)$$

$$AASR_k \approx \frac{\sum\limits_{\substack{q=-\infty \\ q \neq 0}}^{\infty} \int_{-B_p/2}^{B_p/2} G^2(f + q \cdot PRF_k) df}{\int_{-B_p}^{B_p} G^2(f) df}, \quad (23)$$

where *f* is the Doppler frequency.

In the 8th step, the required average transmit power P_{av} is given by

$$P_{av} = \frac{P_t T_r}{PRI_{min}}, \quad (24)$$

where P_t is the peak power and PRI_{min} is the minimum value of all *PRI* for each subswath.

Step 9 verifies whether the normalized equivalent noise figure $NE\sigma^0$ meets the user's requirements. According to

the radar equation, the signal-to-noise ratio (SNR) of SARs operated in scan mode can be written as

$$\frac{S}{N} = \frac{P_t G^2 \lambda^2 \left(\sigma^0 \cdot \frac{l_a}{2} N_B N_L \cdot \rho_{gr}\right)}{(4\pi)^3 B_k T_0 B_r F_n L_s R_{max}^4} \cdot (B_r T_r)$$
$$\cdot \frac{R_{max} \frac{\lambda}{l_a v_s N_B \sqrt{N_L}}}{PRI}, \quad (25)$$

where σ^0 is the normalized radar cross section (RCS), R_{max} is the farthest range between the radar and the scene, B_k is the Boltzmann constant, $T_0 = 290\,K$, F_n is the receiver noise figure, L_s is the system loss, G is the antenna beam center gain, and ρ_{gr} is the ground range resolution. Therefore, the corresponding formula to verify $NE\sigma^0$ is

$$NE\sigma^0 = \frac{2(4\pi)^3 v_s R_{max}^3 B_k T_0 F_n L_s}{\sqrt{N_L} \lambda^3 G^2 \cdot P_{av} \cdot \rho_{gr}}, \quad (26)$$

Finally, whether the data rate f_D meets the requirements is verified by

$$f_D = \frac{CQk_s}{\rho_r} \left(\frac{T_r}{PRI_{min}}\right), \quad (27)$$

where Q is the quantization bit of each sample, ρ_r is the range resolution, and k_s is the oversampling coefficient.

Fig. 1 shows a flowchart of our proposed parameter design method for a small satellite SAR system in scan mode, which summarizes the previous design steps. The proposed system parameter design approach for a small satellite SAR operating in scan mode is applicable for both land scenes and marine scenes.

III. TRANSMIT POWER OPTIMIZATION METHOD BASED ON SEA SURFACE WIND SPEED AND DIRECTION INFORMATION

First, the influence of the wind speed and the wind direction above the sea surface on the backscattering coefficient is discussed. Next, the proposed transmission power optimization method for marine scenes is introduced.

A. INFLUENCE OF WIND SPEED AND WIND DIRECTION ABOVE SEA SURFACE ON BACKSCATTER COEFFICIENT

The sea surface can be seen as a kind of composite rough surface composed of slightly rough surface superimposed on a large wave structure. The large wave structure causes the slightly rough surface to tilt, forming the double-scale model. The small-scale capillary wave component and the large-scale long wave component of the double-scale model correspond to the two types of sea surface backscattering mechanisms under high-frequency electromagnetic waves: Bragg scattering at oblique incidence and specular reflection at near-zero incidence, respectively. For SARs and scatterometers, the incident angle is relatively large; therefore, Bragg scattering is the main scattering component [22], [23].
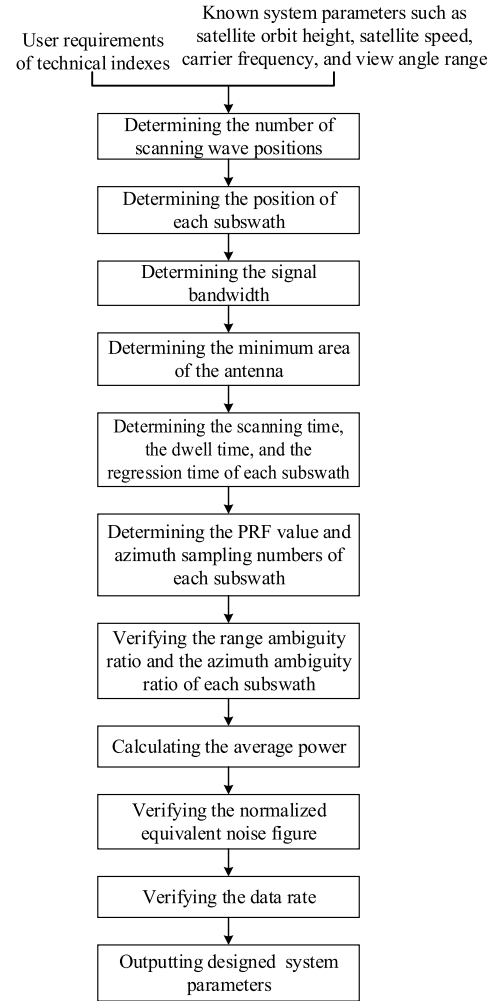

FIGURE 1. Flowchart of the proposed parameter design method for a small satellite SAR system in scan mode.

The Bragg scattering component is expressed as follows:

$$\sigma^0 = 4\pi w_k^4 \cdot \cos^4\theta \left|g_{ij}(\theta)\right|^2 S_{PM}(2w_k \sin\theta, 0), \quad (28)$$

where w_k is the wavenumber, θ is the incidence angle, $g_{ij}(\theta)$ is the first-order scattering coefficient related to the polarization mode, and S_{PM} is the two-dimensional Pierson–Moskowitz (PM) spectrum [24], which is a typical representative wave spectrum. The PM spectrum is a type of gravity spectrum in which long and short gravity waves play a major role when the wavenumbers are different [25]. It is obtained by fitting a large number of ocean observation data after spectral analysis. The PM spectrum model in the main wave direction is:

$$S_{PM}(w_k) = \frac{\alpha}{2w_k^4} \exp\left[-\frac{\beta g^2}{w_k^2 U_{19.5}^4}\right], \quad (29)$$

where $\alpha = 0.0081$, $\beta = 0.74$, g is the gravitational acceleration, and $U_{19.5}$ is the wind speed 19.5 m above the sea surface. When U_{h1}, which is the wind speed at the height of h_1 above the sea surface, is known, the wind speed at the

height of 19.5 m above the sea surface can be obtained by the following conversion:

$$U_{19.5} = U_{h_1} \cdot \left[\begin{array}{c} 1 + 2.5 \lg\left(\frac{19.5}{10}\right) \cdot \\ \left[\sqrt{\dfrac{0.0015}{1 + \exp\left(-\dfrac{U_{h_1} - 1.25}{1.56}\right)}} + 0.00104 \right] \end{array} \right] \quad (30)$$

The two-dimensional PM spectrum can be expressed as:

$$S_{PM}(w_k, \psi) = \frac{\alpha}{2w_k^4} \exp\left(-\frac{\beta g^2}{w_k^2 U_{19.5}^4}\right) \cos^4\left(\frac{\psi - \psi_m}{2}\right), \quad (31)$$

where ψ is the angle between the current direction and the reference direction and ψ_m is the angle between the wind direction and the reference direction. For radar systems operating in HH polarization mode, there are:

$$g_{hh}(\theta) = \frac{\varepsilon_r - 1}{\left[\cos\theta + \left(\varepsilon_r - \sin^2\theta\right)^{1/2}\right]^2}. \quad (32)$$

For radars operating in VV polarization mode, there are:

$$g_{vv}(\theta) = \frac{(\varepsilon_r - 1) \cdot \left[\varepsilon_r \cdot \left[1 + \sin^2\theta\right] - \sin^2\theta\right]}{\left[\varepsilon_r \cos\theta + \left(\varepsilon_r - \sin^2\theta\right)^{1/2}\right]^2}, \quad (33)$$

where ε_r is the relative dielectric constant of seawater.

According to equations (28) and (31), it can be found that the backscattering coefficient of the sea surface has a strong relationship with the wind speed and direction above the sea surface. As the wind speed increases, the backscattering coefficient increases according to the exponential function term in equation (31). The backscattering coefficient is largest when the observation direction is consistent with the wind direction and smallest when the observation direction is perpendicular to the wind direction according to the cosine function term in equation (31).

The mature CMOD5 geophysical model function [26] can also obtain the relationship between the backscattering coefficient and the wind speed and direction. Fig. 2 shows the relationship between the simulated backscatter coefficient and the wind speed, while Fig. 3 shows the relationship between the simulated backscatter coefficient and the wind direction. Figs. 2 and 3 are plotted using the CMOD5 model and verify the characteristics of the relationship between the backscattering coefficient and wind speed and direction summarized above.

B. OPTIMAL CALCULATION OF TRANSMIT POWER
Multimodal small satellite SARs make full use of the flexible scanning and the ability to generate multibeam coverage of phased array antennas and software-reconfigurable technology. By receiving remote control commands from ground stations, remote sensors can be operated in different modes, including the SAR, altimeter, scatterometer and spectrometer.
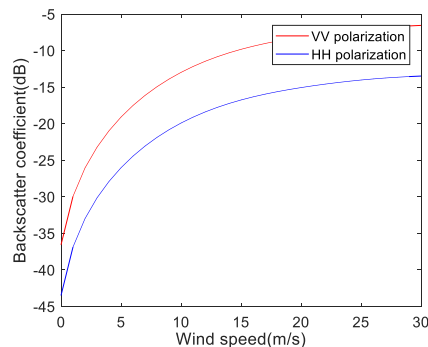
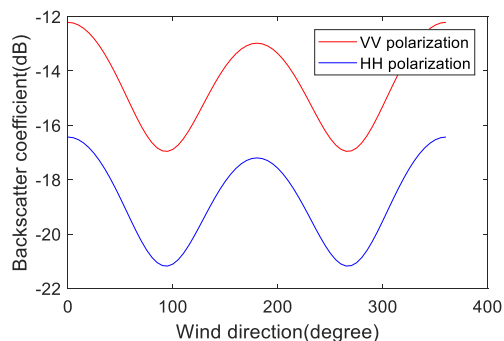**FIGURE 2.** Relationship between the backscattering coefficient and the wind speed.

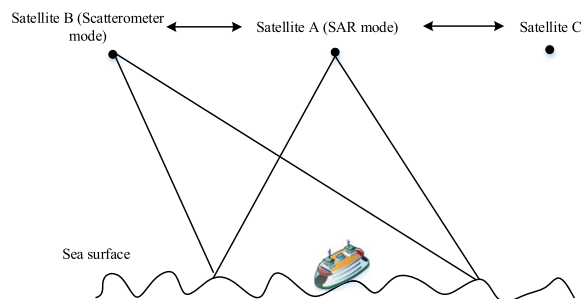**FIGURE 3.** Relationship between the backscattering coefficient and the wind direction.

FIGURE 4. Example diagram of multimodal small satellite synchronous observations.

When the multimodal small satellite SAR is working in scatterometer mode, highly precise information regarding the wind direction and wind speed of the irradiated sea area can be obtained. The microwave scattering intensity on the sea surface is relatively strong when the wind speed in the irradiated sea area is relatively high and the wind direction is appropriate. When other small satellites synchronously observing the sea scene receive information that the wind speed is relatively high and the wind direction is appropriate, they can optimize their own emission power, thus improving the available data sampling time. Fig. 4 shows an example of the above application. Small satellite A is in SAR mode and small satellite B is in scatterometer mode. Both satellites are observing the same sea area at the same time. Small satellite B transmits the retrieved information, including the wind speed, the wind direction, the average backscatter coefficient of sea

surface, etc., to small satellite A. If the wind speed above the irradiated sea area is relatively high and the wind direction is suitable, small satellite A can optimize its own emission power based on the average backscatter coefficient information of the sea surface transmitted by satellite B. The working modes of different satellites at a given time are arranged by receiving remote control instructions from ground stations when satellites pass through the coverage areas of the ground stations. A task scheduling technique needs to be developed to arrange appropriate working modes for different satellites at a given time according to the requirements of the tasks.

According to equation (26), the following can be derived:

$$P_t = \frac{2(4\pi)^3 v_s R_{max}^3 B_k T_0 F_n L_s PRI_{max}}{\sqrt{N_L} \lambda^3 G^2 \cdot \text{NE}\sigma^0 \cdot \rho_{gr} T_r}, \qquad (34)$$

where P_t is the normal signal peak power and PRI_{max} is the maximum PRI among all subswaths. Therefore, the following formula for optimizing the transmission power can be derived:

$$P_t' = \frac{2(4\pi)^3 v_s R_{max}^3 B_k T_0 F_n L_s PRI_{max}}{\sqrt{N_L} \lambda^3 G^2 \cdot \frac{\bar{\sigma'}^0}{\bar{\sigma}^0} \cdot \text{NE}\sigma^0 \cdot \rho_{gr} T_r}, \qquad (35)$$

where P_t' is the optimized signal peak power, $\bar{\sigma}^0$ is the average backscatter coefficient of the sea surface under calm sea conditions, and $\bar{\sigma'}^0$ is the average backscatter coefficient of the sea surface measured by a scatterometer synchronously observing the sea surface. In SAR systems, the movement of a platform inevitably deviates from the nominal motion. These uncertainties of the platform's motion degrade the image quality during imaging [27], [28]. However, the platform's motion uncertainties have little influence on equation (35) since this equation is related to the transmitted signal power rather than the signal phase.

Obviously, when the wind speed above the irradiated sea area is high and the wind direction is appropriate, $\bar{\sigma'}^0$ is notably larger than $\bar{\sigma}^0$, and the required peak signal power can be significantly reduced. Even under the circumstance that a small satellite operating in SAR mode moves toward the wind direction, i.e., the case that the direction of the radar line of sight is perpendicular to the wind direction since SARs normally operate in side view, it is possible to optimize the transmit power as long as the wind speed is high, resulting in that $\bar{\sigma'}^0$ is greater than $\bar{\sigma}^0$.

In summary, the system adaptively operates with the appropriate transmit power according to the scattering intensity of the illuminated sea. A small satellite working in SAR mode receives information such as the wind speed, the wind direction, and the average backscatter coefficient of the sea surface transmitted by another small satellite that synchronously observes the same area and operates in the scatterometer mode. Then, the optimized transmit power is calculated using equation (35) according to the information that the small satellite receives, and the small satellite transmits at the calculated power.

IV. SIMULATION AND RESULTS OF OCEAN SCENE IMAGING FOR SMALL SATELLITE SARS IN SCAN MODE

Several simulation experiments were conducted. The main goals included two aspects: (1) verifying the rationality of the proposed system parameter design method; and (2) verifying the correctness of the proposed transmission power optimization method. First, the sea surface simulation method, point target echo simulation and imaging processing method are introduced. Second, the design results of system parameters of the small satellite SAR system in scan mode are provided. Third, the imaging simulation results of ocean scenes under conventional transmission power are given to verify the rationality of the parameter design results. Finally, the simulation results of ocean scene imaging with optimized transmit power are reported to verify the correctness of the proposed transmit power optimization method.

A. SEA SURFACE SIMULATION METHOD ADOPTED

To simulate ocean scene echo for small satellite SAR systems, a sea surface simulation is the first requirement. At present, the main method for sea surface simulation is to generate the wave spectrum and then simulate the sea surface according to the generated wave spectrum. The wave spectrum is the power density spectrum of the sea surface, which is the Fourier transform of the correlation function of sea surface height fluctuation. Common wave spectra include PM spectrum, JONSWAP spectrum and Apel spectrum. In this paper, the PM spectrum, which is mathematically the most concise, is used to simulate the sea surface.

After obtaining the two-dimensional PM spectrum given in equation (31), the two-dimensional sea surface simulation can be completed using the following two-dimensional inverse Fourier transform:

$$f(x_m, y_n) = \frac{1}{L_x L_y} \cdot \sum_{m_k=-M/2+1}^{M/2} \sum_{n_k=-N/2+1}^{N/2} \left\{ S_{PM}\left(K_{m_k}, K_{n_k}\right) \right.$$
$$\left. \cdot \exp\left[j\left(K_{m_k} x_m + K_{n_k} y_n\right)\right] \right\}, \qquad (36)$$

where x_m and y_n represent the range and the azimuth coordinates of the two-dimensional sea surface, respectively, L_x and L_y represent the length of the two-dimensional sea surface in the range and azimuth directions respectively, M and N represent the number of sampling points in the range and azimuth directions respectively, and $S_{PM}\left(K_{m_k}, K_{n_k}\right)$ represents the PM spectrum in the two-dimensional frequency domain.

B. POINT TARGET ECHO SIMULATION AND IMAGING PROCESSING METHOD ADOPTED

At present, the main methods for simulating sea echo include the time domain and frequency domain algorithms [29]. The frequency domain algorithm has higher computational efficiency, while the time domain algorithm has higher accuracy. In this study, the time domain algorithm [30] was chosen for simulation.

TABLE 1. Technical indicators of small satellite SAR in scan mode.

Ground range resolution	15 m	Azimuth resolution	15 m
Lower limit of swath	49 km	Upper limit of swath	81 km
Range ambiguity to signal ratio	<-20 dB	Azimuth ambiguity to signal ratio	<-20 dB
System Sensitivity	<-20 dB	Data rate	<10 Mbps

TABLE 2. Known technical parameters in the parameter design process.

Orbit height	530 km	View angle range	20°-50°
Earth radius	6371 km	Pulse width	10 µs
Satellite speed	7600 m/s	Peak power	2100 W
Carrier frequency	9.6 GHz	Noise figure	5 dB
System loss	7 dB	Receiver guard time	10 µs
Initial view angle	35°	Multilook number	1
Azimuth antenna	⩽4.5 m	Range antenna	⩽1.344 m

According to the principle of scan SARs, the echo signal of a point target can be expressed as follows:

$$
\begin{aligned}
&s(\tau, t) \\
&= \sigma \cdot \sum_n \text{rect}\left[\frac{t - n \cdot PRI}{T_D}\right] \cdot \text{rect}\left[\frac{\tau - \frac{2R(t)}{C}}{T_r}\right] \\
&\quad \cdot \exp\left[-j\pi \frac{4R(t)}{\lambda}\right] \cdot \exp\left\{j\pi k_r \left[\tau - \frac{2R(t)}{C}\right]^2\right\}, \quad (37)
\end{aligned}
$$

where τ is the range time, t is the total time, σ is the backscattering coefficient of the point target, rect() represents the rectangle function, T_D is the beam dwell time, $R(t)$ is the instantaneous slant distance, and k_r is the modulation frequency of the transmitted signal.

After simulating the height change of the two-dimensional sea surface, the backscattering coefficient of each cell can be calculated by using the wind speed, wind direction, incidence angle, etc. After calculating the instantaneous slant range from each cell on the sea surface to the radar, the echo data of the sea surface can be obtained by superposing the echo signals of each cell according to the scattering coefficient matrix and the impulse response function of the system. After the echo matrix is obtained, the SPECAN imaging algorithm [31], which is suitable for scan mode, is adopted for imaging to obtain the sea surface SAR image.

C. SYSTEM PARAMETER DESIGN RESULTS OF SCAN MODE

Table 1 gives the technical indicator requirements for small satellite SAR in scan mode, and Table 2 gives the known technical parameters. Note that the parameters listed in Tables 1 and 2 refer to the parameters to be adopted in an ongoing development plan. According to these parameters, using the proposed system parameter design method, the system parameter output results shown in Table 3 are obtained. It is noted that the nearly 80 W average power listed in Table 3 is acceptable for minisatellites (100-500 kg) [32].

Table 4 lists the calculated results of the spatial position and beam pointing angle of each subswath. Table 5 shows the residence time, the regression time and the scanning time for each subswath.

Combinations of different wave positions and PRF were selected for verification; then whether the combination of different wave positions and PRF meets the requirements of indicators such as ambiguity to signal ratio and data rate

TABLE 3. Output results of system parameters designed.

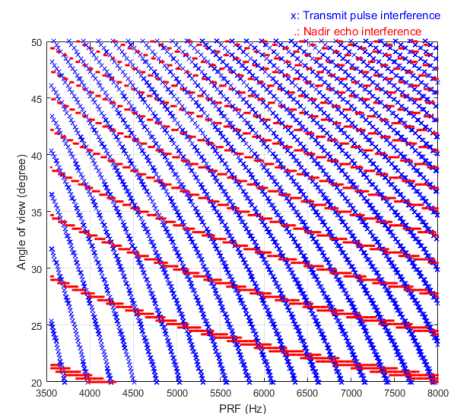| Azimuth antenna	4.28 m	Range antenna	0.81 m
PRF minimum	3555.5 Hz	PRF maximum	14615.4 Hz
Signal bandwidth	17.4 MHz	Antenna area	⩾2.87 m²
Number of wave positions	7	Average power	79.4 W

FIGURE 5. The timing diagram for selecting the proper PRF.

can be judged. The verification results are shown in Table 6, which shows that the calculated results all meet the requirements of the index. Table 7 shows the calculated PRF values and the number of PRF samples for each subswath. Fig. 5 plots the corresponding timing diagram for selecting the proper PRF.

D. SIMULATION RESULTS OF OCEAN SCENES AT CONVENTIONAL TRANSMITTING POWER

Using the two-dimensional PM spectrum model, the two-dimensional sea surface was simulated, and the results are shown in Fig. 6. The wind direction angles corresponding to Fig. 6 (a), (b), (c), and (d) are 45°, 45°, 90°, and 0°, respectively. The wind speeds corresponding to Fig. 6 (a), (b), (c), and (d) are 10 m/s, 15 m/s, 10 m/s, and 5 m/s, respectively. The simulation area size is set to 1024 m × 1024 m.

Comparing Fig. 6 (a) with Fig. 6 (b), it can be found that when the wind speed increases, the sea surface fluctuation

TABLE 4. Output results of spatial position and beam pointing angle of each subswath.

	Subswath 1	Subswath 2	Subswath 3	Subswath 4	Subswath 5	Subswath 6	Subswath 7
Lower view angle (°)	35	35.8	36.57	37.3	38.01	38.69	39.35
Incidence angle (°)	38.41	39.32	40.19	41.03	41.84	42.62	43.37
Ground range width (km)	13.4	13.14	12.9	12.68	12.48	12.29	12.12
Closet slant rage (km)	656.65	664.13	671.61	679.10	686.58	694.09	701.54
Distant slant range (km)	664.97	672.46	679.94	687.42	694.90	702.38	709.86
Center range (km)	660.79	668.27	675.76	683.24	690.72	698.20	705.69
Beam width (degree)	0.92	0.88	0.84	0.81	0.78	0.75	0.72
Width in slant range direction (km)				8.32			
Total ground distance (km)				81.32			

TABLE 5. Output results of dwell time, regression time and scanning time of each subswath.

	Subswath 1	Subswath 2	Subswath 3	Subswath 4	Subswath 5	Subswath 6	Subswath 7
Dwell time (s)	0.091	0.092	0.093	0.094	0.095	0.096	0.097
Regression time (s)	0.598	0.605	0.611	0.618	0.625	0.632	0.638
Scanning time (s)	0.688	0.696	0.704	0.712	0.720	0.727	0.735

TABLE 6. Verification results of different wave positions and PRF combinations.

Parameters	1	2	3	4
Central view angle (degrees)	35	35.8	37.3	38
minimum view angle (degrees)	34.54	35.36	36.89	37.61
maximum view angle (degrees)	35.46	36.24	37.71	38.39
PRF (Hz)	3800	3800	4000	4000
Range ambiguity to signal ratio (dB)	-43.95	-43.71	-44.32	-43.45
Azimuth ambiguity to signal ratio (dB)	-63.00	-63.00	-64.09	-64.09
System sensitivity (dB)	-22.18	-22.14	-22.21	-22.15
Data rate (Mbps)	4.77	4.67	4.75	4.68

TABLE 7. Output results of PRF values and PRF samples of each subswath.

Number of azimuth samples transmitted in the air		18	19	20	21	22	23
Subswath 1	PRF (Hz)	3883.36	4111.8				
	azimuth samples	352	372				
Subswath 2	PRF (Hz)	3839.60	4065.45				
	azimuth samples	352	372				
Subswath 3	PRF (Hz)			4020.16	4243.51		
	azimuth samples			372	393		
Subswath 4	PRF (Hz)				4196.75	4417.63	
	azimuth samples				393	414	
Subswath 5	PRF (Hz)				4151.02	4396.49	
	azimuth samples				392	414	
Subswath 6	PRF (Hz)					4322.4	4538.52
	azimuth samples					414	434
Subswath 7	PRF (Hz)					4276.31	
	azimuth samples					414	

and roughness become larger. Comparing Fig. 6 (a) with Fig. 6 (c), it can be found that when the wind direction angle is 90°, the sea surface fluctuation is slightly lower than when the wind direction angle is 45°. The above phenomena coincide with the theoretical law.

After the two-dimensional simulated sea surface was obtained, a sea surface simulation imaging experiment was carried out according to the parameters of the satellite platform and the radar. Based on the echo simulation and imaging processing methods described in Section IV.B, the echo signal of the whole sea surface was obtained first; then, the sea surface image in scan mode was obtained. Fig. 7 shows the sea surface imaging results. The wind direction angles corresponding to Fig. 7 (a), (b), (c), and (d) are 45°, 45°,
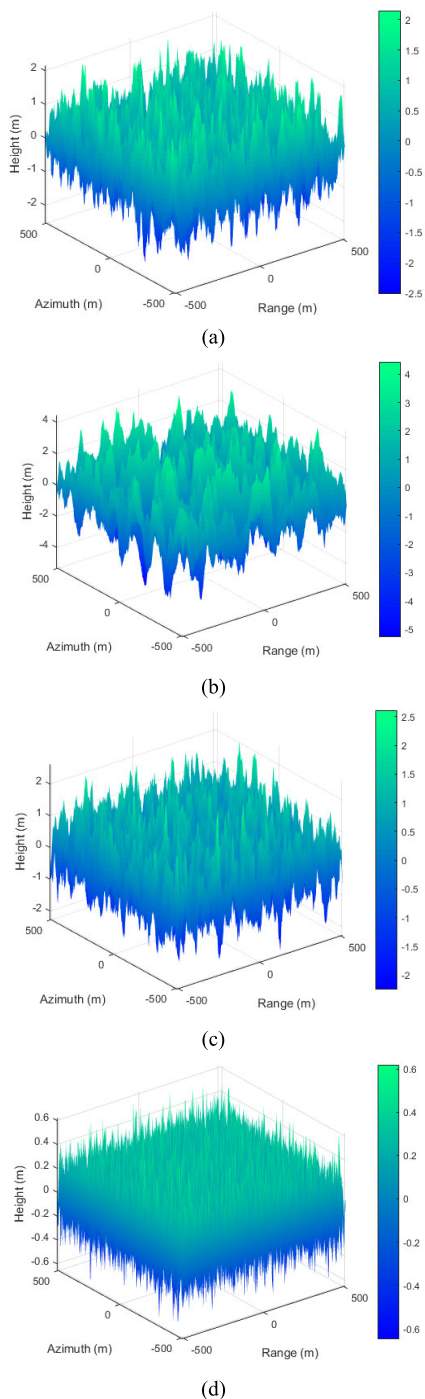
FIGURE 6. Simulation results of a two-dimensional sea surface: (a) Wind direction angle 45°, wind speed 10 m/s; (b) Wind direction angle 45°, wind speed 15 m/s; (c) Wind direction angle 90°, wind speed 10 m/s; (d) Wind direction angle 0°, wind speed 5 m/s.
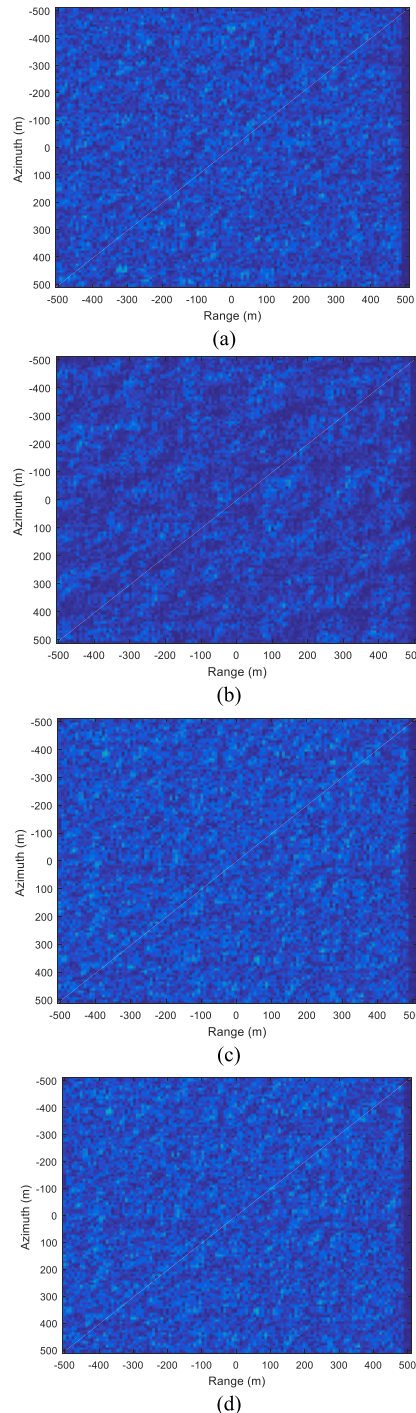

FIGURE 7. Sea surface imaging results in scan mode: (a) Wind direction angle 45°, wind speed 10 m/s; (b) Wind direction angle 45°, wind speed 15 m/s; (c) Wind direction angle 90°, wind speed 10 m/s; (d) Wind direction angle 0°, wind speed 5 m/s.

90°, and 0°, respectively. The wind speeds corresponding to Fig. 7 (a), (b), (c), and (d) are 10 m/s, 15 m/s, 10 m/s, and 5 m/s, respectively.

As shown in Fig. 7, good sea surface imaging results can be obtained under different wind speeds and wind directions when using the designed radar parameters, and clear sea wave stripes can be seen.

In addition, simulation experiments of ship imaging both with and without sea clutter were also conducted. We artificially set an area with a very low RCS in the upper-left corner of the simulated marine scene to facilitate the calculation of the SNR values. Noise was added according to the bandwidth and the noise figure of the receiver listed in Tables 2 and 3,
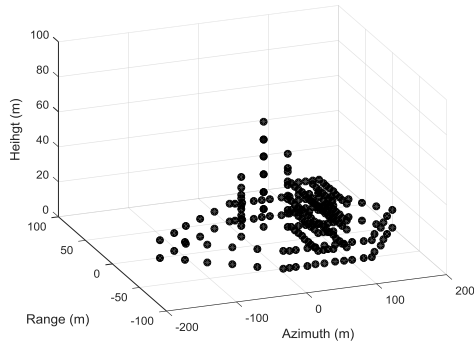
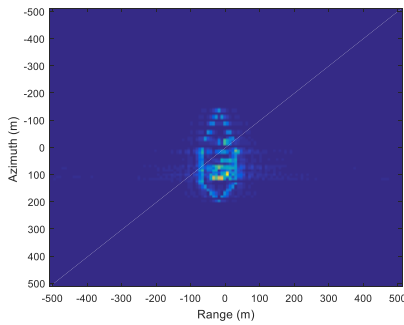**FIGURE 8.** Scatter diagram of the ship used in the simulation.

FIGURE 9. Simulation result of ship imaging without sea clutter in scan mode.

respectively. Fig. 8 shows a scatter diagram of a simulated ship. Fig. 9 shows the result of the ship imaging simulation without sea clutter, and Fig. 10 plots the results of the ship imaging simulation in a sea scene. The wind direction angles corresponding to Fig. 10 (a), (b), (c), and (d) are 45°, 45°, 90°, and 0°, respectively. The wind speeds corresponding to Fig. 10 (a), (b), (c), and (d) are 10 m/s, 15 m/s, 10 m/s, and 5 m/s, respectively. Note that to ensure a better ship display effect, Figs. 9 and 10 show only the sea surface images near the ship.

From Figs. 9 and 10, it can be seen that the experiment using the designed radar parameters achieved good imaging results under different wind speeds and directions, thus verifying the rationality of the designed radar parameters.

## E. SIMULATION RESULTS OF OCEAN SCENES WITH OPTIMIZED TRANSMIT POWER

The average backscattering coefficient of the sea surface in a calm sea state was set to −23 dB. According to the parameters set in the simulation and equation (24), the calculated average emission power is 79.4 W. When the wind direction angle is 45° and the wind speed is 10 m/s, the average backscattering coefficient of the sea surface is −14 dB, and the average transmitting power of the radar can be reduced to 10 W. When the wind direction angle is 45° and the wind speed is 15 m/s, the average backscattering coefficient of the sea surface is −12 dB, and the average transmitting power of the radar can be reduced to 6.3 W. When the wind direction angle is 90° and the wind speed is 10 m/s, the average backscattering coefficient of the sea surface is −17 dB, and
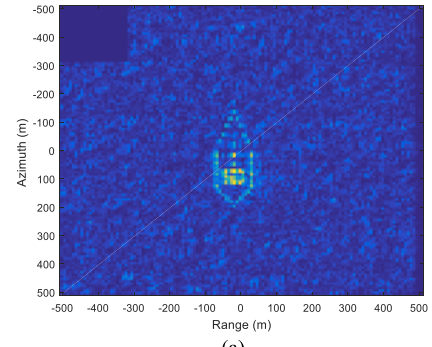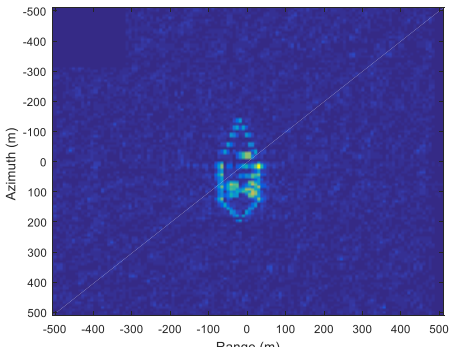

(a)
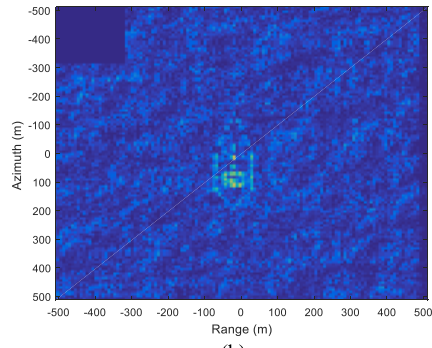
(b)
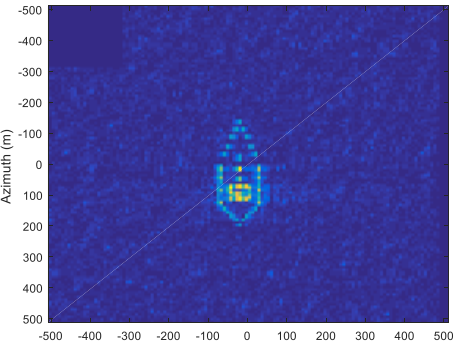
(c)

(d)

FIGURE 10. Composite imaging results of ships and sea surface in scan mode: (a) Wind direction angle 45°, wind speed 10 m/s; (b) Wind direction angle 45°, wind speed 15 m/s; (c) Wind direction angle 90°, wind speed 10 m/s; (d) Wind direction angle 0°, wind speed 5 m/s.

the average transmitting power of the radar can be reduced to 19.9 W. When the wind direction angle is 0° and the wind speed is 5 m/s, the average backscattering coefficient of the
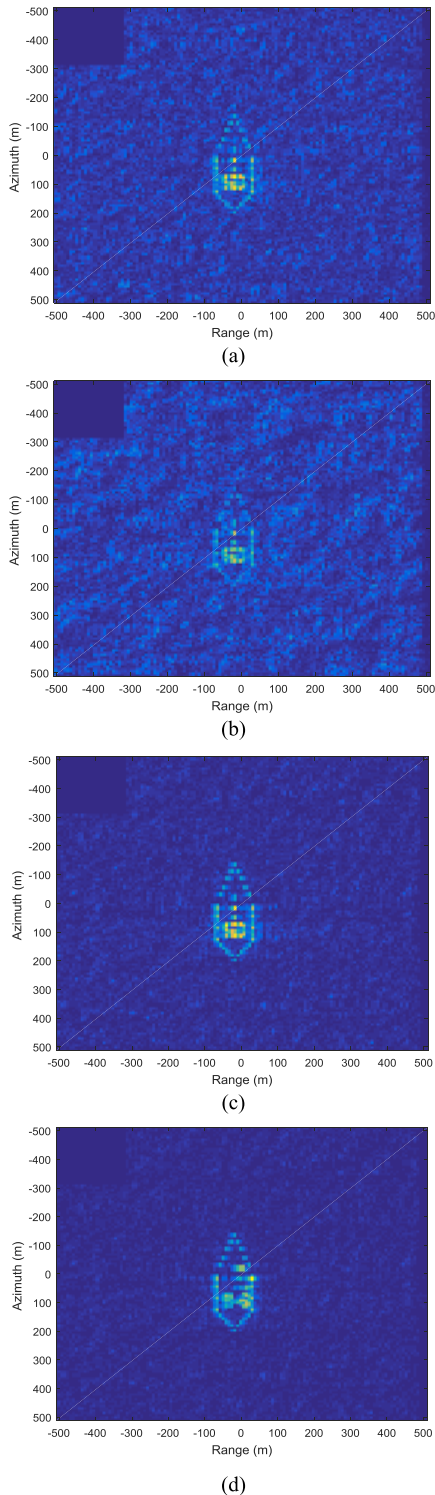
(a)

(b)

(c)

(d)

FIGURE 11. Composite imaging results of ship and sea surface after optimization of transmission power: (a) Wind direction angle 45°, wind speed 10 m/s; (b) Wind direction angle 45°, wind speed 15 m/s; (c) Wind direction angle 90°, wind speed 10 m/s; (d) Wind direction angle 0°, wind speed 5 m/s.

sea surface is −18 dB, and the average transmitting power of the radar can be reduced to 25 W. Fig. 11 shows a composite imaging result of the ship and the sea surface after the

TABLE 8. SNR and SCR related to Figs. 10 and 11.

Figure	SNR (dB)	SCR (dB)
Fig. 10 (a)	33.9	9.3
Fig. 10 (b)	33.8	7.2
Fig. 10 (c)	33.9	12.4
Fig. 10 (d)	33.7	13.3
Fig. 11 (a)	24.9	9.2
Fig. 11 (b)	23	7.1
Fig. 11 (c)	27.9	12.1
Fig. 11 (d)	28.9	13.1

TABLE 9. Image entropy and contrast related to Figs. 10 and 11.

Figure	Entropy (bit)	Contrast
Fig. 10 (a)	4.3278	291.0017
Fig. 10 (b)	4.6682	295.7879
Fig. 10 (c)	3.4242	268.1662
Fig. 10 (d)	3.1251	257.1372
Fig. 11 (a)	4.3277	290.9943
Fig. 11 (b)	4.6707	296.4066
Fig. 11 (c)	3.4604	269.0941
Fig. 11 (d)	3.0991	256.6392

transmission power is optimized. The wind direction angles corresponding to Fig. 11 (a), (b), (c), and (d) are 45°, 45°, 90°, and 0°, respectively. The wind speeds corresponding to Fig. 11 (a), (b), (c), and (d) are 10 m/s, 15 m/s, 10 m/s, and 5 m/s, respectively.

Comparing Fig. 10 (a)–(d) with Fig. 11 (a)–(d), respectively shows that although the image quality decreases slightly after optimizing the transmission power, the wave stripes and the ship outline in the image are still relatively clear.

Table 8 presents the SNR and the signal-to-clutter ratio (SCR) related to Figs. 10 and 11. It can be seen that the SCR values are not related to the transmitted signal power and that the SNR values after the power optimization are still high enough. These phenomena conform to the theoretical expectations because the signal power and the clutter power are in direct proportion to the transmit power and because the normalized RCS of a ship's scatterer is generally far greater than the normalized equivalent noise figure of SAR systems. That is, the SNR value after the transmit power optimization is still high with the relatively small reduction of the transmit power.

Table 9 gives the image entropy and the image contrast of Figs. 10 and 11. It can be seen that the values of the image entropy and the image contrast after power optimization are roughly equal to the values before power optimization. In other words, the image quality has not decreased significantly after power optimization.

V. CONCLUSION

Multimodal small satellite SAR is a new type of radar system under development that can work in SAR, altimeter, scatterometer, and spectrometer modes in a time-shared manner. When applied to marine scenes, this approach can

achieve measurements of both marine targets and marine dynamic environments with high precision. The ability to simulate multimodal small satellite SAR using computer systems is an important foundation for related research into this new system. In this study, an imaging simulation of ocean scenes and the optimization of emission power for multimodal small satellite SAR in scan imaging mode were investigated—primarily the system parameter design method for multimodal small satellite SAR in scan mode, the imaging simulation of ocean scenes and the optimization method of emission power based on wind speed and wind direction information of the sea surface. Various simulation experiments were carried out. The simulation results showed that when the designed system parameters were used for an imaging simulation of scan mode, good imaging results of ocean scenes were obtained. In addition, the simulation results also verify that when the sea surface wind speed is relatively high and the wind direction is suitable, a relatively good imaging result of the ocean scene can be obtained even when using reduced emission power.

ACKNOWLEDGMENT

REFERENCES

[1] W. Lv, P. Zhou, Y. Wang, X. Zhang, Y. Wan, and X. Qu, "Parameter design of multi-mode small satellite SAR system," in *Proc. IEEE Int. Geosci. Remote Sens. Symp. (IGARSS)*, Yokohama, Japan, Jul. 2019, pp. 8617–8620.

[2] S. Y. Kim, J. B. Sung, and A. Torre, "In-orbit antenna pattern extraction method for active phased-array SAR antennas," *IEEE Antennas Wireless Propag. Lett.*, vol. 15, pp. 317–320, 2016.

[3] T. V. Fepeussi, N. Testi, Y. Xu, and Y. Jin, "High-accuracy narrowband software-defined radar using successive multiple-frequency continuous-wave modulation for sensing applications," *IEEE Trans. Microw. Theory Techn.*, vol. 67, no. 9, pp. 3917–3927, Sep. 2019.

[4] P. Liu, J. Mendoza, H. Hu, P. G. Burkett, J. V. Urbina, S. Anandakrishnan, and S. G. Bilen, "Software-defined radar systems for polar ice-sheet research," *IEEE J. Sel. Topics Appl. Earth Observ. Remote Sens.*, vol. 12, no. 3, pp. 803–820, Mar. 2019.

[5] S. Neemat, F. Uysal, O. Krasnov, and A. Yarovoy, "Reconfigurable range-Doppler processing and range resolution improvement for FMCW radar," *IEEE Sensors J.*, vol. 19, no. 20, pp. 9294–9303, Oct. 2019.

[6] W. Ao, F. Xu, Y. Li, and H. Wang, "Detection and discrimination of ship targets in complex background from spaceborne ALOS-2 SAR images," *IEEE J. Sel. Topics Appl. Earth Observ. Remote Sens.*, vol. 11, no. 2, pp. 536–550, Feb. 2018.

[7] J. Yang and J. Zhang, "Accuracy assessment of HY-2A scatterometer wind measurements during 2011–2017 by comparison with buoys, ASCAT, and ERA-interim data," *IEEE Geosci. Remote Sens. Lett.*, vol. 16, no. 5, pp. 727–731, May 2019.

[8] W. Lin, X. Dong, M. Portabella, S. Lang, Y. He, R. Yun, Z. Wang, X. Xu, D. Zhu, and J. Liu, "A perspective on the performance of the CFOSAT rotating fan-beam scatterometer," *IEEE Trans. Geosci. Remote Sens.*, vol. 57, no. 2, pp. 627–639, Feb. 2019.

[9] D. Hauser, C. Tison, T. Amiot, L. Delaye, N. Corcoral, and P. Castillan, "SWIM: The first spaceborne wave scatterometer," *IEEE Trans. Geosci. Remote Sens.*, vol. 55, no. 5, pp. 3000–3014, May 2017.

[10] S. Gao, Y. Rahmat-Samii, R. E. Hodges, and X.-X. Yang, "Advanced antennas for small satellites," *Proc. IEEE*, vol. 106, no. 3, pp. 391–403, Mar. 2018.

[11] K. Iwamoto, T. Araki, Y. Kobayashi, H. Sawada, T. Ito, T. Sano, Y. Takeshita, S. Ota, M. Ueno, K.-I. Shibata, T. Nakao, H. Komatsu, and K. Iwamoto, "Experimental verifications on small optical inter-satellite communication system for small and micro satellites," in *Proc. IEEE Int. Conf. Space Opt. Syst. Appl. (ICSOS)*, Naha, Japan, Nov. 2017, pp. 59–62.

[12] F. Zhang, X. Yao, H. Tang, Q. Yin, Y. Hu, and B. Lei, "Multiple mode SAR raw data simulation and parallel acceleration for Gaofen-3 mission," *IEEE J. Sel. Topics Appl. Earth Observ. Remote Sens.*, vol. 11, no. 6, pp. 2115–2126, Jun. 2018.

[13] W. Pitz and D. Miller, "The TerraSAR-X satellite," *IEEE Trans. Geosci. Remote Sens.*, vol. 48, no. 2, pp. 615–622, Feb. 2010.

[14] J.-C. Jang, K.-A. Park, A. A. Mouche, B. Chapron, and J.-H. Lee, "Validation of sea surface wind from sentinel-1A/B SAR data in the coastal regions of the korean peninsula," *IEEE J. Sel. Topics Appl. Earth Observ. Remote Sens.*, vol. 12, no. 7, pp. 2513–2529, Jul. 2019.

[15] X. Liu, P. Zhou, X. Zhang, W. Sun, and Y. Dai, "The parameter design results of near space airship SAR system," in *Proc. IEEE Int. Geosci. Remote Sens. Symp. (IGARSS)*, Beijing, China, Jul. 2016, pp. 1102–1105.

[16] L. Zheng, L. Shuhao, and W. Yuekun, "System design of GEO-LEO bistaic SAR with high resolution and wide swath," in *Proc. IEEE Int. Conf. Mechatronics, Robot. Autom. (ICMRA)*, Hefei, China, May 2018, pp. 1–5.

[17] M. Denny and D. Thom, "SAR key parameter calculation tool," in *Proc. RADAR*, Edinburgh, U.K., Oct. 2002, pp. 380–384.

[18] Y. Wang and D. Yao, "Analysis of some key parameters in sliding spotlight SAR," in *Proc. IET Conf. Publications*, Guilin, China, Apr. 2009, pp. 1–4.

[19] K. Tomiyasu, "Conceptual performance of a satellite borne, wide swath synthetic aperture radar," *IEEE Trans. Geosci. Remote Sens.*, vol. GE-19, no. 2, pp. 108–116, Apr. 1981.

[20] J. Chen, G.-C. Sun, M. Xing, J. Yang, C. Ni, Y. Zhu, W. Shu, and W. Liu, "A parameter optimization model for geosynchronous SAR sensor in aspects of signal bandwidth and integration time," *IEEE Geosci. Remote Sens. Lett.*, vol. 13, no. 9, pp. 1374–1378, Sep. 2016.

[21] Z. Ding, W. Yin, T. Zeng, and T. Long, "Radar parameter design for geosynchronous SAR in squint mode and elliptical orbit," *IEEE J. Sel. Topics Appl. Earth Observ. Remote Sens.*, vol. 9, no. 6, pp. 2720–2732, Jun. 2016.

[22] V. N. Kudryavtsev, S. Fan, B. Zhang, A. A. Mouche, and B. Chapron, "On quad-polarized SAR measurements of the ocean surface," *IEEE Trans. Geosci. Remote Sens.*, vol. 57, no. 11, pp. 8362–8370, Nov. 2019.

[23] C.-C. Lin, W. Lengert, and E. Attema, "Three generations of C-band wind scatterometer systems from ERS-1/2 to MetOp/ASCAT, and MetOp second generation," *IEEE J. Sel. Topics Appl. Earth Observ. Remote Sens.*, vol. 10, no. 5, pp. 2098–2122, May 2017.

[24] J. V. Toporkov and G. S. Brown, "Numerical simulations of scattering from time-varying, randomly rough surfaces," *IEEE Trans. Geosci. Remote Sens.*, vol. 38, no. 4, pp. 1616–1625, Jul. 2000.

[25] Z. Chen and Y. Zhang, "Offshore electromagnetic spectrum distribution prediction model based on ray tracing method and PM wave spectrum," *IEEE Access*, vol. 7, pp. 174298–174311, 2019.

[26] H. Hersbach, A. Stoffelen, and S. de Haan, "An improved C-band scatterometer ocean geophysical model function: CMOD5," *J. Geophys. Res.*, vol. 112, no. C3, pp. 1–18, Mar. 2007.

[27] Y. Zha, W. Pu, Y. Huang, and J. Yang, "Fast factorized back projection imaging algorithm integrated with motion error estimation for bistatic forward-looking SAR," *IEEE J. Sel. Topics Appl. Earth Observ. Remote Sens.*, vol. 12, no. 10, Oct. 2019, pp. 3949–3965.

[28] W. Pu, Y. Huang, J. Wu, H. Yang, and J. Yang, "Fast compressive sensing-based SAR imaging integrated with motion compensation," *IEEE Access*, vol. 7, pp. 53284–53295, 2019.

[29] Y. Liu, W. Wang, S. Dai, B. Rao, and G. Wang, "A unified multimode SAR raw signal simulation method based on acquisition mode mutation," *IEEE Geosci. Remote Sens. Lett.*, vol. 14, no. 8, pp. 1233–1237, Aug. 2017.

[30] D. A. G. Dell'Aglio, G. Di Martino, A. Iodice, D. Riccio, and G. Ruello, "A unified formulation of SAR raw signals from extended scenes for all acquisition modes with application to simulation," *IEEE Trans. Geosci. Remote Sens.*, vol. 56, no. 8, pp. 4956–4967, Aug. 2018.

[31] J. Holzner and R. Bamler, "Burst-mode and ScanSAR interferometry," *IEEE Trans. Geosci. Remote Sens.*, vol. 40, no. 9, pp. 1917–1934, Sep. 2002.

[32] H. Saito, B. Pyne, K. Tanaka, M. Mita, T. Kaneko, J. Hirokawa, T. Tomura, H. Watanabe, P. R. Akbar, and K. Ijichi, "Proto-flight model of SAR for 100kg class small satellite," in *Proc. AIAA/USU Conf. Small Satellites*, Logan, UT, USA, Aug. 2019, pp. 1–7.

PENG ZHOU (Member, IEEE) received the B.S. degree in electronic engineering and the M.S. degree in automation control engineering from the China University of Petroleum, Dongying, China, in 1997 and 2000, respectively, and the Ph.D. degree in signal and information processing from the University of Electronic Science and Technology of China, Chengdu, China, in 2008.

From December 2017 to November 2018, he worked as a Visiting Researcher with the Department of Information Engineering, University of Pisa, Italy. He is currently an Associate Professor with the College of Oceanography and Space Informatics, China University of Petroleum, Qingdao, China. His current research interests include SAR imaging, ISAR imaging, and especially topics related to radar imaging of ships.

WEIQIANG LV received the B.S. degree in electronics and information engineering from the Shandong University of Science and Technology, Qingdao, China, in 2016. He is currently pursuing the M.S. degree with the College of Oceanography and Space Informatics, China University of Petroleum, Qingdao. His research interests include the parametric design of synthetic aperture radars and radar imaging.

ZHENHUA ZHANG received a Ph.D. degree in signal processing from Xidian University, Xi'an, China, in 2007. He is currently a Researcher with the Beijing Research Institute of Telemetry, Beijing, China. His current research interests include SAR imaging and radar signal processing.

YING WANG received the M.S. degree in signal processing from Xidian University, Xi'an, China, in 2005. He is currently a Senior Engineer with the Beijing Research Institute of Telemetry, Beijing, China. His current research interests include radar signal processing and SAR systems.

XI ZHANG received the B.S. degree in information systems from the Qingdao University of Science and Technology, Qingdao, China, in 2005, and the M.S. degree in signal and information processing and the Ph.D. degree in computer science from the Ocean University of China, Qingdao, in 2008 and 2011, respectively.

He is currently an Associate Researcher with the First Institute of Oceanography, Ministry of Natural Resources of the People's Republic of China, Qingdao. His current research interests include the remote sensing of oceans and SAR imaging.

YONGSHOU DAI received the B.S. degree in automation control engineering from the China University of Petroleum, Dongying, China, in 1986, the M.S. degree in computer science from Beijing Jiaotong University, Beijing, China, in 1992, and the Ph.D. degree in automation control engineering from the University of Science and Technology Beijing, Beijing, in 2007.

He is currently a Professor with the College of Oceanography and Space Informatics, China University of Petroleum. His current research interests include remote sensing information acquisition and signal processing.

• • •